Volume 1 | Number 1 | Jan 2013 | Pages 1–100

Nanoscale

www.rsc.org/nanoscale

ROYAL SOCIETY OF CHEMISTRY

www.rsc.org/nanoscale

Journal Name

ARTICLE

Novel Phosphorus Doped Carbon Nitride Modified TiO$_2$ Nanotube Arrays with Improved Photoelectrochemical Performance

Jingyang Su,[a] Ping Geng,[b] Xinyong Li,[c] Qidong Zhao,[c] Xie Quan [c] and Guohua Chen [a, b*]

Novel phosphorus-doped graphitic-carbon nitride (P-C$_3$N$_4$) modified vertically aligned TiO$_2$ nanotube arrays (NTs) were designed and synthesized. They can significantly enhance the conduction and utilization of photogenerated charge carriers of TiO$_2$ NTs. The heterostructure was successfully fabricated through a three-step process: electrochemical anodization and wet-dipping followed by thermal polymerization. The prepared P-C$_3$N$_4$/TiO$_2$ NTs exhibit enhanced light-absorption characteristics and improved charge separation and transfer ability, thus resulting in a 3-fold photocurrent (1.98 mA cm^{-2} at 0 V vs Ag/AgCl) compared with that of pure TiO$_2$ NTs (0.66 mA cm^{-2} at 0 V vs Ag/AgCl) in 1 M NaOH solution. The prepared P-C$_3$N$_4$/TiO$_2$ NTs photoelectrodes also present excellent photocatalytic and photoelectrocatalytic capabilities in the degradation of methylene blue (MB). The kinetics rate of P-C$_3$N$_4$/TiO$_2$ NTs in photoelectrocatalytic process for MB is 2.7 times that of pristine TiO$_2$ NTs. Furthermore, the prepared sample was used as a photoanode for solar-driven water splitting, giving a H$_2$ evolution rate of 36.6 μmol h^{-1} cm^{-2} at 1.0 V vs RHE under simulated solar light illumination. This novel structure with the rational design for visible light response shows potential for metal free materials in photoelectrochemical applications.

Introduction

Highly ordered, vertically oriented TiO$_2$ nanotube arrays (TiO$_2$ NTs) obtained by Ti metal anodization have attracted wide interest because of their impressive properties. Various applications of TiO$_2$ NTs have been explored in such fields as pollutants degradation,[1-5] sterilization,[6, 7] water splitting,[8-12] dye-sensitized solar cells [13-16] and gas sensors.[17-19] Compared with traditional TiO$_2$ nanocrystal-based nanofilms, the unique structure of nanotube arrays provides convenience for the separation and transfer of photo-generated charges and possesses higher photon collection efficiency.[9, 20] However, the practical application of TiO$_2$ NTs is significantly hindered by its wide band gap (3.2 eV for anatase), which limits the photoresponse of TiO$_2$ to the UV region (λ < 385 nm, less than 5% of the solar spectrum). Recently, semiconductors with narrower band gaps, such as CdS,[21-23] CdSe[24, 25, 24, 25,] Cu$_2$O,[26, 27] Fe$_2$O$_3$,[28, 29] AgBr,[30] ZnFe$_2$O$_4$,[31] and Fe$_2$TiO$_5$ [32] were

investigated to improve the photoresponse of TiO$_2$ NTs in the visible region through the formation of a heterostructure coupling TiO$_2$ with the above-mentioned narrow band gap semiconductors.

Graphitic carbon nitride (g-C$_3$N$_4$) is a new kind of non-metallic π-conjugated polymeric materials with a band gap of 2.7 eV, as reported by Wang et al. in 2009.[33] Many reports have demonstrated that it is able to produce hydrogen or oxygen from water splitting and organic degradation under visible light irradiation.[33-35] Especially, g-C$_3$N$_4$ possesses superior reduction ability due to the high potential of the conduction band (-1.42 V vs Ag/AgCl, pH 6.6),[36] which makes it a fine material to couple with TiO$_2$ for efficient charge transfer and separation. However, in spite of the advantages of this metal free material as an excellent semiconductor, the poor adaption of the material interfaces and grain boundary effects hinder its electric charge transport.[37-40] To overcome this challenge, chemical doping is adopted as an effective strategy to improve the performance by modifying their electronic structure and surface properties. Recently, phosphorus-doped g-C$_3$N$_4$ (P-C$_3$N$_4$) was developed by a co-condensation strategy. As a result, the electronic features of P-C$_3$N$_4$ were altered by this heteroatom doping, providing better electric conductivity up to 4 orders of magnitude.[40] Based on previous studies, a novel heterostructure will be designed in this study by modifying TiO$_2$ NTs in-situ with phosphorus-doped graphitic carbon nitride (P-C$_3$N$_4$). The heterojunction built between P-C$_3$N$_4$ and TiO$_2$ NTs is expected not only to benefit light absorption, but also to improve separation of photogenerated electrons and inhibit the electron-

a. Environmental Engineering Program, School of Engineering, The Hong Kong University of Science and Technology, Clear Water Bay, Kowloon, Hong Kong, China
b. Department of Chemical and Biomolecular Engineering, The Hong Kong University of Science and Technology, Clear Water Bay, Kowloon, Hong Kong, China
c. Key Laboratory of Industrial Ecology and Environmental Engineering (Ministry of Education, China), School of Environmental Science and Technology, Dalian University of Technology, Dalian 116024, China
* Email: kechengh@ust.hk
† Electronic Supplementary Information (ESI) available:
See DOI: 10.1039/x0xx00000x

hole pair recombination, which can enhance the photoelectrochemical activity of the P-C$_3$N$_4$/TiO$_2$ NTs significantly. Methylene blue (MB) will be used as the model pollutant for photocatalytic and photoelectrocatalytic degradation reactions to evaluate the photoelectrochemical capability of the as-prepared P-C$_3$N$_4$/TiO$_2$ NTs photoelectrodes under solar light irradiation. Moreover, P-C$_3$N$_4$/TiO$_2$ NTs will be employed as photoanode for photoelectrochemical water splitting under solar light illumination. Detailed analysis is given subsequently.

Experimental Section

Chemicals

All the chemicals are used as received without further treatment. Ammonium fluoride [NH$_4$F] (>99.99%), dicyandiamide [CN] (>99.9%), 2-aminobenzonitrile [ABN] (>99.9%), 1-butyl-3-methylimidazolium hexafluorophosphate [BmimPF$_6$] (>99.9%) were purchased from Aladdin. Ethylene glycol [EG] (>99.5%) was obtained from Scharlan and methylene blue [MB] (>99%) was procured from Sigma. MilliQ water (deionized water, 18 MΩ) was used for the preparation of all the solutions.

Photoelelctrodes preparation

TiO$_2$ NTs were fabricated by a two-step anodization process. Prior to anodization, the Ti foils were first degreased by sonicating in acetone, ethanol and DI water, respectively, followed by drying in air stream for 30 minutes. The anodization process was carried out in a conventional two-electrode system with the Ti foil as the anode and a Pt foil as the cathode. The electrolyte consisted of 0.5 wt% NH$_4$F and 2 vol% water in EG solution. All the anodization process was carried out at room temperature of 25 ^{o}C. In the first-step anodization, the Ti foil was anodized at 60 V for 60 min, and then the as-grown nanotubes layer was ultrasonically removed in 1 M HCl solution. The produced Ti foil then underwent the second anodization at 60 V for 30 min, producing a nanoring-nanotube structure. After the two-step anodization, the prepared TiO$_2$ NTs samples were cleaned with DI water and dried with nitrogen gas for 30 minutes. Then the anodized TiO$_2$ NTs samples were annealed in air at 450°C for 2 h with a heating rate of 2°C min^{-1} for phase conversion from amorphous to crystalline.

P-C$_3$N$_4$/TiO$_2$ NTs were prepared by a facile wet-dipping method (Scheme 1). CN and ABN were used as precursors to produce graphitic carbon nitride. The incorporation of phenylene groups produced by ABN into g-C$_3$N$_4$ can improve the p-electron delocalization in the conjugated system, and thus changes the intrinsic optical and electronic properties of the resulting CN-ABN polymers, resulting in much enhanced photo-response compared with pristine g-C$_3$N$_4$.[41] BmimPF$_6$ was added into the solution as a phosphorous source. In a typical synthetic procedure, the prepared TiO$_2$ NTs were dipped into solution containing the precursor (CN: ABN: BmimPF$_6$ = 100: 1: 1) with desired concentration (1 to 5 mg mL^{-1}). After 12 h dipping saturation, the electrode was taken out of the solution
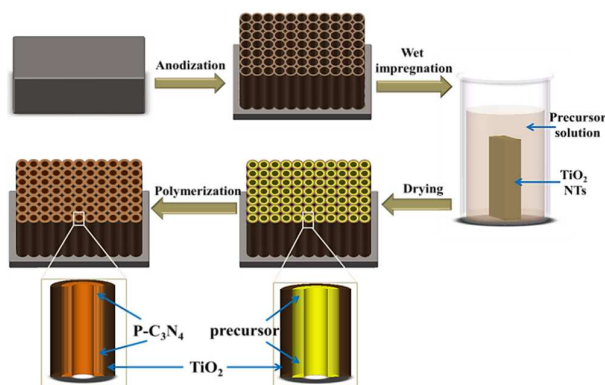
and dried in a nitrogen gas stream for 30 minutes. Afterwards, the electrode was heated to 540°C in an argon atmosphere with a heating rate of 2.3^{o}C min^{-1} and kept at this temperature for another 2 h to produce P-C$_3$N$_4$/TiO$_2$ NTs heterostructure. For comparison, some pure TiO$_2$ NTs were also treated under the same conditions.

Characterization

Surface morphologies of TiO$_2$ NTs and P-C$_3$N$_4$/TiO$_2$ NTs were examined by Field Emission Scanning Electron Microscopy (FESEM, JEOL 6700F). The structure and shape of the P-C$_3$N$_4$/TiO$_2$ NTs were also examined by a High Resolution Transmission Electron Microscope (HRTEM, JEOL JEM2010F), combining with energy dispersive X-ray spectroscopy (EDX) for the determination of element composition. The accelerating voltage was 200 kV in each case. X-ray Diffraction (XRD) analysis was conducted by X-Ray diffractometer (PANalytical, X'pert Pro) equipped with a Cu Kα radiation source (wavelength of 1.54 Å), mainly for the study of structural properties of crystalline materials in modified thin films. The diffractograms were recorded with a 2θ range of 10 ~ 80° with a normal scan speed of 0.05°s^{-1}. X-ray Photoelectron Spectroscopy (XPS) was recorded on a PHI 5600 (Physical Electronic, USA) equipped with an Al monochromatic X-ray source. C 1s line at 284.6 eV was used as the calibration reference before each measurement. UV-vis Diffuse Reflectance Spectra (DRS) were recorded on a Shimadzu UV-2500PC UV-vis spectrometer with a diffuse reflectance accessory, and BaSO$_4$ was used as the reference sample (100% reflectance). Photoluminescence spectra (PL) were measured at room temperature of 25 ^{o}C on a Shimadzu RF-5301 PC spectrometer using a 325 nm excitation light.

Photoelectrochemical Test

Photoelectrochemical measurements were performed using a conventional three-electrode cell system and an electrochemical workstation (PGSTAT 100, Autolab, Netherlands). The prepared electrode was employed as the working electrode. Meanwhile, a saturated Ag/AgCl electrode and a platinum electrode served as the reference and counter electrode, respectively. All the potentials were referred to the saturated Ag/AgCl unless otherwise stated. Some 1 M NaOH was used as

Scheme 1 Synthesis procedure of P-C$_3$N$_4$/TiO$_2$ NTs photoelectrode

ARTICLE

the electrolyte. A 300 W high-pressure Xenon short arc lamp (Newport) was used as the simulated solar light source to provide a light intensity of 100 mW cm^{-2}, which was calibrated prior to every photoelectrochemical test using a calibrated Si photodiode. I-V curves were measured at a scanning rate of 50 mV s^{-1}. Electrochemical impedance spectroscopy (EIS) was documented in the frequency range of 0.01 to 10^5 Hz with an AC voltage amplitude of 10 mV at a bias of 0 V (vs the Ag/AgCl) in 1 M NaOH solution.

Photoelectrochemical performance test

Photoelectrocatalytic degradation of MB was performed in a standard three-electrode configuration and an electrochemical workstation (PGSTAT 100, Autolab, Netherlands). P-C$_3$N$_4$/TiO$_2$ NTs photoelectrode was employed as the working electrode, Pt foil as the counter electrode, and a saturated Ag/AgCl as the reference electrode. A 300 W high-pressure Xenon short arc lamp (Newport) was used as the simulated solar light source to provide a light intensity of 100 mW cm^{-2}. All the experiments were performed using 0.1 M Na$_2$SO$_4$ as the electrolyte with magnetic stirring. The initial concentration of the MB aqueous solution was 10 mg L^{-1}. The changes in MB concentration were monitored by measuring the maximal absorption at λ = 664 nm using an UV-vis spectrophotometer (Unico UV-2102 PC, USA). Photoelectrochemical water splitting reaction for hydrogen and oxygen production was conducted in a three electrode system where the reaction vessel was connected to a glass-closed gas-circulation system. The reaction solution was maintained at room temperature using a flow of cooling water during the reaction. The evolved gases were analyzed using a gas chromatograph (GC, Tianmei GC-7900T) equipped with a thermal conductive detector. All the data were obtained after repeating the same experiments for at least 3 times with insignificant difference observed.

Results and discussion

Figure 1A presents the top-down SEM image of TiO$_2$ NTs after the second anodization. The nanorings structure on the top is uniform in a large scale, with a smooth surface observed. Typical top-view and side-view images of P-C$_3$N$_4$/TiO$_2$ NTs were displayed in Figure 1B and inset, respectively, indicating that P-C$_3$N$_4$ was dispersed uniformly without blocking the channels. The pore diameter of TiO$_2$ NTs became smaller after P-C$_3$N$_4$ modification, revealing a tube-in-tube structure formed after P-C$_3$N$_4$ deposition. The length of NTs was determined as around 5 μm, which can guarantee an effective light absorption and efficient charge separation.[42, 43] The microscopic structure of the P-C$_3$N$_4$/TiO$_2$ NTs heterostructure was further investigated by TEM and HRTEM. Figure 1C is a typical TEM image of the TiO$_2$ NTs after the modification of P-C$_3$N$_4$, showing that the P-C$_3$N$_4$ formed from thermal polymerization is dispersed on the inner walls of the TiO$_2$ NTs, which is consistent with the FESEM images. After P-C$_3$N$_4$ thermal polymerization, the TiO$_2$ NTs still show good crystallization (Figure 1E). The observed lattice plane is 0.351 nm, which is consistent with (101) plane of anatase TiO$_2$. Moreover, an

obvious boundary of P-C$_3$N$_4$ layer and TiO$_2$ layer is revealed in Figure 1F. TEM-EDX mapping spectrum (SI, Figure S1) presents a uniform distribution of titanium, oxygen, carbon, nitrogen and phosphorus, demonstrating the presence of P-C$_3$N$_4$. In addition, the TEM line-EDX (Figure 1D) clearly shows that there is considerable inner diffusion of the elements across the interface over P-C$_3$N$_4$/TiO$_2$ NTs structure. Moreover, there is a concentration gradient of Ti and O in the walls of nanotubes, with the average distribution of C and N in the inner walls of nanotubes, demonstrating uniform dispersion of P-C$_3$N$_4$ in the inner wall.

The elemental compositions and chemical status of the P-C$_3$N$_4$/TiO$_2$ NTs were further analyzed by XPS. The XPS survey spectrum (Figure 2A) of the P-C$_3$N$_4$/TiO$_2$ NTs confirmed the existence of Ti, O, C, N and P elements. Figures 2 B-C indicate the presence of Ti 2p and O 1s in the prepared samples with corresponding peaks at 459.0 eV and 464.8 eV for Ti 2p, and 530.1 eV for O 1s. It is notable that after P-C$_3$N$_4$ deposition, a small negative shift (ca. 0.15 eV) of Ti 2p$_{3/2}$ can be identified, which is due to the electron transfer from P-C$_3$N$_4$ to TiO$_2$ NTs, indicating a heterojunction formed successfully between TiO$_2$ and P-C$_3$N$_4$. Figure 2D shows the high-resolution C 1s XPS spectra of P-C$_3$N$_4$/TiO$_2$ NTs. As can be seen from this figure, the C 1s peak at 284.6 eV can be ascribed to carbon and defect-containing sp^2-hybridized carbon atoms present in graphitic domains. The C 1s peak at 286.1 eV is assigned to the C-C bond in the turbostratic CN structure. The peak at 288.1 eV is
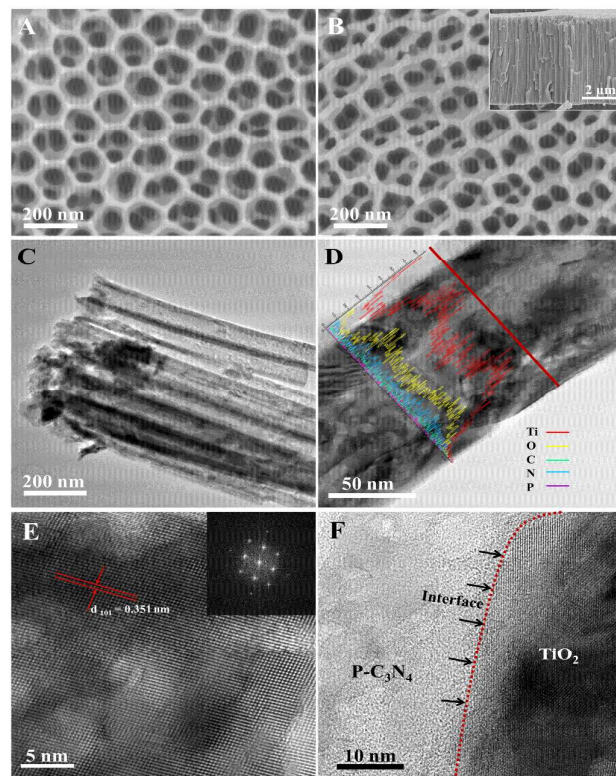

Figure 1 SEM images of pristine TiO$_2$ NTs (A) and P-C$_3$N$_4$/TiO$_2$ NTs (B); representative TEM images (C, D) and line-EDX of P-C$_3$N$_4$/TiO$_2$ NTs (D); HRTEM images of P-C$_3$N$_4$/TiO$_2$ NTs showing the good crystallinity of TiO$_2$ (E, inset is corresponding SAED) and interface between TiO$_2$ and P-C$_3$N$_4$ (F)
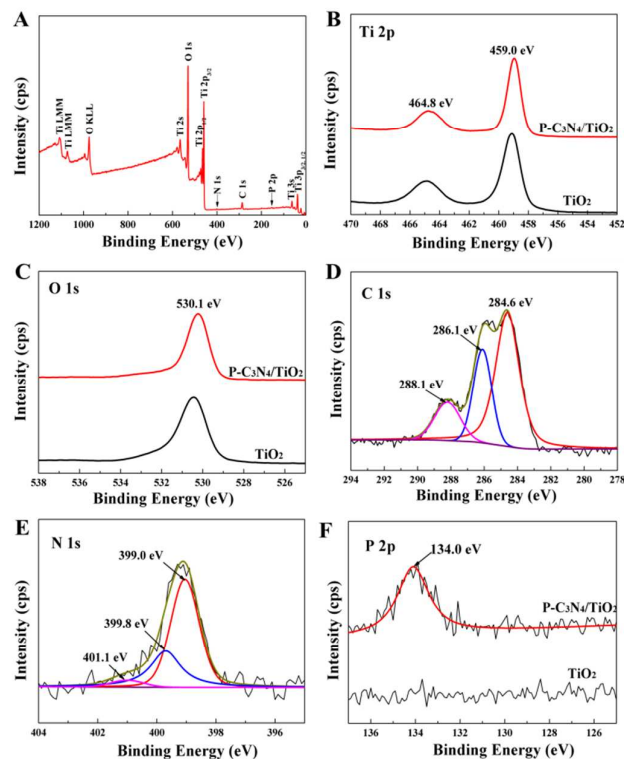
Nanoscale Accepted Manuscript

Figure 2 XPS survey spectrum (A) and corresponding core levels of Ti 2p (B), O 1s (C), C 1s (D), N 1s (E) and P 2p (F) of P-C_3N_4/TiO_2 NTs

ascribed to the sp^3 C-N bond of the sp^3 bonded composition. Figure 2E shows the high-resolution N 1s XPS spectra of the P-C_3N_4/TiO_2 NTs. The asymmetrical and broad features of the observed N 1s XPS peaks suggest the coexistence of distinguishable models. The main N 1s peak at the binding energy of 399.0 eV can be assigned to sp^2-hybridized nitrogen (C-N-C). The two weak peaks at about 399.8 and 401.1 eV can be attributed to tertiary nitrogen (N-$(C)_3$) and amino functional groups having a hydrogen atom (C-N-H), respectively.[44] The presence of the N-$(C)_3$ groups confirms the polymerization of dicyandiamide. The existence of amino functional groups suggests that the g-C_3N_4 product prepared by pyrolysis of dicyandiamide was incompletely condensed, which is consistent with the previous reports.[44, 45] Moreover, the area ratio of N-$(C)_3$ and C-N-H peaks also suggests that the degree of condensation reaction and the molar percentage are about 85% and 15%, respectively. Also, the structural details on the incorporation of P into the g-C_3N_4 scaffold were obtained with XPS measurements (Figure 2F). The P 2p binding energy peaks of P-C_3N_4 are centered at 134.0 eV, which is typical for a P-N coordination, while that of pristine TiO_2 NTs shows negligible contributions.[40]

The crystal structure of the P-C_3N_4/TiO_2 NTs heterostructure was revealed by XRD analysis (Figure 3A). For comparison, the XRD patterns from pure TiO_2 NTs and P-C_3N_4 bulk are also shown. All peaks in the curve can be well-indexed by TiO_2 anatase phase (JCPDS No. 71-1167) and Ti metal phase (JCPDS No. 44-1294), which are originated from the TiO_2 NTs
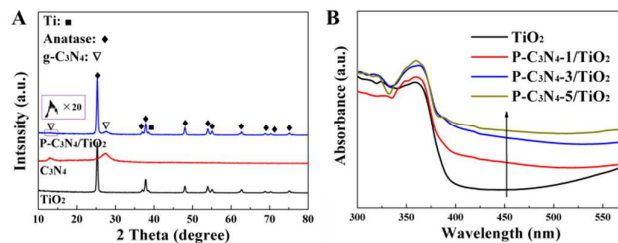

Figure 3 (A) XRD patterns of TiO_2, P-C_3N_4 and P-C_3N_4/TiO_2; (B) DRS spectra of TiO_2 and P-C_3N_4 modification with different precursor solutions

and Ti substrate, respectively. Compared to the TiO_2 NTs, the XRD pattern of the P-C_3N_4/TiO_2 NTs shows that there are two additional peaks at 13.2^o and 27.6^o corresponding to the (110) and (200) crystal planes of g-C_3N_4, respectively.

DRS spectra obtained from the pure TiO_2 NTs show that TiO_2 primarily absorbs ultraviolet light with a maximum absorption wavelength of around 360 nm, which is ascribed to the charge transfer process from the valence band formed by the 2p orbital of the oxide anions to the conduction band formed by the 3d$_{t2g}$ orbital of the Ti^{4+} cations. The as-prepared P-C_3N_4/TiO_2 decorated TiO_2 NTs are denoted as P-C_3N_4-X/TiO_2 (with X being precursor concentration). It is notable that with the increase in precursor concentration, the absorption in the visible region of P-C_3N_4/TiO_2 NTs increased significantly, revealing the excellent light absorption ability of g-C_3N_4 under visible light illumination. The result indicates that visible-light absorption of the TiO_2 NTs is obviously enhanced by introducing P-C_3N_4.

Figure 4 shows the J-V curves of photocurrent density versus the applied potential for the TiO_2 NTs, and P-C_3N_4/TiO_2 NTs prepared under different concentrations. It is obvious that the maximum photocurrent density of 1.98 mA cm^{-2} (P-C_3N_4-3/TiO_2 NTs) is obtained at 0 V vs Ag/AgCl for the P-C_3N_4/TiO_2 NTs electrode, while only 0.66 mA cm^{-2} for pure TiO_2 NTs is observed. This result indicates that the separation rate of photogenerated holes and electrons increased due to the formation of a heterostructure. It is notable that although light absorption of P-C_3N_4-5/TiO_2 is a little higher than that of P-C_3N_4-3/TiO_2, the formed thick and dense P-C_3N_4 layer blocks some light absorption of TiO_2 NTs (as indicated
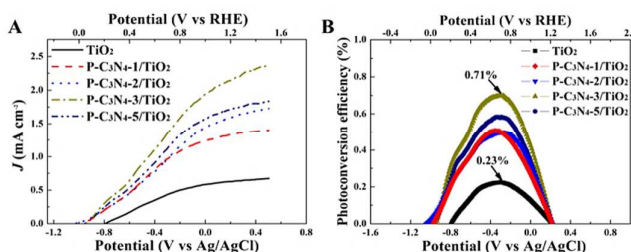

Figure 4 Photoelectrochemical properties of P-C_3N_4/TiO_2 NTs and TiO_2 NTs photoelectrodes: (a) J-V collected with a scan rate of 20 mV s^{-1} in the dark and under illumination; (b) photoconversion efficiency as a function of the applied potential

ARTICLE

by the decreased light absorption in the UV region of DRS spectra) and hinder the electron transport ability of TiO_2 NTs. Thus, P-C_3N_4-3/TiO_2 gives the optimal photocurrent.

The photoconversion efficiency of the P-C_3N_4/TiO_2 photoelectrode was calculated using the following equation (1): where η is the photoconversion efficiency, I is the photocurrent density (mA cm^{-2}), J_{light} is the incident light irradiance (mW cm^{-2}), E^0_{rev} is the standard reversible potential which is 1.23 V vs. RHE, and V is the applied bias potential vs RHE. Figure 4B presents the plots of the photoconversion efficiency vs. applied bias potentials. The optimal photoconversion efficiency can be up to 0.71% at -0.3 V vs Ag/AgCl for P-C_3N_4/TiO_2 NTs, while pristine TiO_2 NTs can only achieve photoconversion efficiency of 0.23% at -0.35 V vs Ag/AgCl. Furthermore, photoelectrochemical stability of prepared samples was also demonstrated by testing their chopped transient photocurrent density versus time at 0 V (SI, Figure S3). It is clearly that nearly no decrease of photocurrent was observed for all the prepared samples. Especially, P-C_3N_4-3/TiO_2 generated the highest photocurrent of 1.96 mA cm^{-2} among all the samples, which was around 3.0 times greater than the values obtained on TiO_2 NTs.

In order to explore the effect of incorporation of phenylene groups from ABN into g-C_3N_4, DRS spectra of g-C_3N_4 prepared from different precursors of CN and CN: ABN = 100: 1 were provided for comparison (SI, Figure S4). As one can see, after introduction of ABN, optical absorption of the resulted CN-ABN$_{0.01}$ was enhanced in the visible region, which benefits photo-response due to the improvement of π-electron delocalization in the formed CN-ABN co-polymer.[41]

Furthermore, we compared P-C_3N_4/TiO_2 using CN and CN-ABN$_{0.01}$ as different precursors. Clearly, much enhanced light absorption both in UV and visible regions can be observed after the incorporation of phenylene groups when using CN-ABN$_{0.01}$ as precursors (SI, Figure S5), which is beneficial to improved PEC performance of the produced P-C_3N_4/TiO_2. The prepared P-C_3N_4/ TiO_2 NTs with CN-ABN$_{0.01}$ as precursors exhibit much higher photocurrent than that with CN only. At 0 V vs Ag/AgCl, P-C_3N_4/TiO_2 NTs (CN-ABN$_{0.01}$) show 40% enhancement of photocurrent than that of P-C_3N_4/TiO_2 NTs from CN only (1.4 mA cm^{-2} at 0 V vs Ag/AgCl) (SI, Figure S6). To identify the roles of g-C_3N_4 and P doping in the formed P-C_3N_4/TiO_2, charge separation and transfer abilities of g-C_3N_4/TiO_2 NTs (without P doping) and P-C_3N_4/TiO_2 NTs were evaluated by EIS and PL (Figure 5). Comparing typical EIS Nyquist plots of the
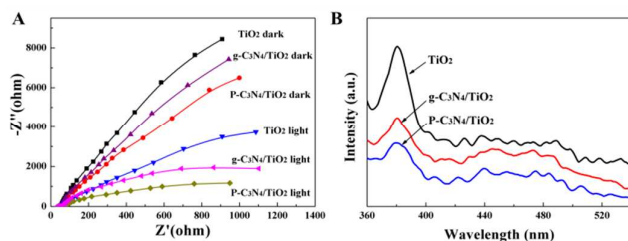
TiO_2 NTs, g-C_3N_4/TiO_2 NTs and P-C_3N_4/TiO_2 NTs under dark and light irradiation, one can see that both of the radiuses of the arc on the EIS Nyquist plots of the g-C_3N_4/TiO_2 and P-C_3N_4/TiO_2 NTs in the dark are much lower than that of pristine TiO_2 NTs. This indicates that the charge transfer resistance decreases after the modification of g-C_3N_4 and P-C_3N_4. The decrease in resistance reveals that the wet-dipping and polymerization technique employed here gives rise to a good interaction between C_3N_4 (both g-C_3N_4 and P-C_3N_4) and the TiO_2 NTs (with better ohmic contacts), and consequently leads to an efficient and fast charge transfer path from the C_3N_4/TiO_2 NTs heterojunction to the Ti substrate. Under light irradiation, the arc radius on the EIS Nyquist plot of the P-C_3N_4/TiO_2 NTs is still much smaller than those of pristine TiO_2 and g-C_3N_4/TiO_2, which indicates an effective separation of photogenerated electron-hole pairs and fast interfacial charge transfer to the electron donor/electron acceptor after TiO_2 NTs is modified by P-C_3N_4 under light irradiation. These results show that after P doping, produced P-C_3N_4/TiO_2 NTs exhibit enhanced charge separation ability than pristine g-C_3N_4/TiO_2 NTs, which is due to significantly enhanced electric conductivity by introduction of P heteroatoms. From PL spectra, one can see that the photoluminescence intensities of TiO_2 NTs decrease with the modification of the g-C_3N_4, and it further decreased after P doping, which reveals that the addition of heterojunction and introduction of P heteroatoms decreases the density of the charge recombination for luminescence. The formed P-C_3N_4 can act as traps to capture the photo-induced electrons from TiO_2 NTs, and thus effectively inhibit the recombination of electron-hole pairs, leading to much enhanced photoelectrochemical activity than g-C_3N_4/TiO_2 and pristine TiO_2 NTs (SI, Figure S7).

To gain more in-depth understanding of the charge-transport properties of P-C_3N_4/TiO_2 and pristine TiO_2 NTs, the electron recombination kinetics of these two types of NTs were further investigated by monitoring the transient open-circuit voltage (V_{oc}) as a function of time upon turning off the illumination. Under open-circuit conditions, electrons accumulate within the nanostructured semiconductor films following solar light irradiation and shifting the apparent Fermi level to negative potentials. Once the illumination is stopped, the accumulated electrons are slowly discharged because they are scavenged by redox species in the electrolyte. The electron density in the conduction band decays sharply due to charge recombination, with the V_{oc} decay rate directly determined by the recombination rate. Figure 6A depicts the V_{oc} decay as a
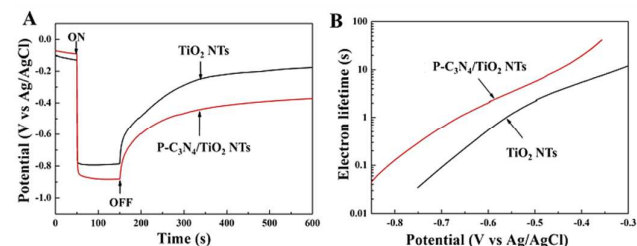

Figure 5 (A) EIS responses of pristine TiO_2 NTs, g-C_3N_4/TiO_2 NTs and P-C_3N_4/TiO_2 NTs under dark and with solar light illumination; (B) PL spectra of TiO_2 NTs, g-C_3N_4/TiO_2 NTs and P-C_3N_4/TiO_2 NTs with excitation light wavelength of 325 nm at room temperature

Figure 6 (A) Open circuit potential of the pristine TiO_2 and P-C_3N_4/TiO_2 NTs under simulated solar light irradiation. (B) The corresponding electron lifetimes as a function of open circuit potential

function of time measured on the pristine and P-C_3N_4/TiO_2 NTs anodes. It is evident that the P-C_3N_4/TiO_2 NTs electrode has a significantly slower V_{oc} decay rate than that of pristine TiO_2 NTs, suggesting slower recombination kinetics in P-C_3N_4/TiO_2 NTs. Based on the V_{oc} decay rate, the lifetime of photogenerated electrons (τ_n), i.e. the average time that the photogenerated electrons exist before they recombine, can be calculated by the following expression:

$$\tau_n = -(k_BT/e)(dV_{oc}/dt)^{-1} \tag{2}$$

where k_B is Boltzmann's constant, T the temperature, and e the elementary charge. The calculated τ_n is plotted in Fig. 6B as a function of V_{oc} for the two types of anodes. It is observed that τ_n of the P-C_3N_4/TiO_2 NTs is longer than that of pristine TiO_2 NTs. The extended τ_n observed in P-C_3N_4/TiO_2 NTs compared with that of TiO_2 NTs may be attributed to surface defects, which act as adsorption sites benefiting charge carrier transportation.

Methylene blue (MB) was selected as a target pollutant to evaluate the photocatalytic performance of P-C_3N_4/TiO_2 heterostructure. Figure 7A presents MB removals in various degradation processes, i.e. the photoelectrocatalytic (PEC) process, the photocatalytic (PC) process, the electrochemical (EC) process, the direct photolysis and dark control processes. As shown in Figure 7, 92.8% of MB removal rate was obtained after 60 min of PEC process, while only 52% and 1.8% of MB were removed in PC and EC process within the same time, respectively. The kinetic constant is 0.040 min^{-1} for PEC process, 2.4 times of that in PC process (0.017 min^{-1}). The PEC removals of MB on P-C_3N_4/TiO_2 NTs and TiO_2 NTs were also performed and the results are shown in Figure 7B. About 92.8% MB was removed on P-C_3N_4/TiO_2 NTs after only 60 min, with a corresponding kinetic constant being 0.040 min^{-1}, 2.7 times of that of TiO_2 NTs. The results show that P-C_3N_4, as a charge collector, can improve the charge transfer and separation in a PEC process.

Figure 8A shows the TOC removal efficiency during MB degradation over P-C_3N_4/TiO_2 NTs and TiO_2 NTs. For P-C_3N_4/TiO_2 NTs, the initial TOC value of MB is 4.77 mg L^{-1}, which reduced to 2.16 mg L^{-1} after 1 h degradation, and further decreased to only 1.07 mg L^{-1} at 2 h reaction. The TOC removal efficiency was 77.6%, nearly 3 times of that observed for pure TiO_2 NTs (26.3%), demonstrating better mineralization ability of P-C_3N_4/TiO_2 NTs as a photocatalyst than pure TiO_2 NTs. The stability of P-C_3N_4/TiO_2 NTs was tested by degrading MB with the same electrode for 5 consecutive times. During 5

Figure 8 (A) TOC removal efficiency of MB on TiO_2 and P-C_3N_4/TiO_2 during PEC degradation process at different time; (B) Removal efficiency of MB with one P-C_3N_4/TiO_2 NTs photoelectrode for 5 consecutive times over 60 min (0.5 V vs Ag/AgCl, light intensity is 100 mW cm^{-2})

repeated PEC cycles, the MB removal efficiency remained almost unchanged (Figure 8B), indicating good stability of P-C_3N_4/TiO_2 photoelectrode when applied as an anode for degradation of pollutants. Additionally, the produced OH· under solar light illumination over P-C_3N_4/TiO_2 was captured using DMPO and recorded by ESR spectra at ambient temperature in an aqueous dispersion (SI, Figure S9). Four characteristic peaks of DMPO-OH· with intensity 1:2:2:1 can be clearly observed showing that efficient hydroxyl radicals were produced on P-C_3N_4/TiO_2 under solar light irradiation, while no peaks observed in dark. The results display that hydroxyl radicals can be generated efficiently on the prepared samples under solar light, which is beneficial to MB removal and mineralization with high efficiency.

It is important to directly examine the evolution of H_2 and O_2 for the prepared samples in a PEC water-splitting process. For this purpose, photoelectrocatalytic water splitting reaction for hydrogen and oxygen production was conducted in a three electrode system under vacuum atmosphere. The evolved gases were sampled and injected into a gas chromatograph in-situ for quantitative analysis. The results showed that under simulated solar light irradiation H_2 was evolved on the surface of electrode with a generation rate of 36.6 μmol h^{-1} within the testing period of 5 h (Figure 9). The photocurrent was also given in the inset of Figure 9, demonstrating excellent stability of the prepared sample in aqueous solution. Additionally, even after 6 months storage, the prepared samples show nearly the same performance as observed from the chopped J-V current under solar
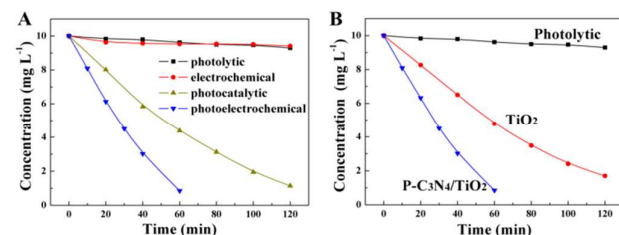

Figure 7 (A) Degradation of MB solutions by different processes with the as-prepared P-C_3N_4/TiO_2 NTs electrode (B) Degradation of MB solutions by TiO_2 and prepared P-C_3N_4/TiO_2 with the bias of 0.5 V under solar light illumination (light intensity is 100 mW cm^{-2})
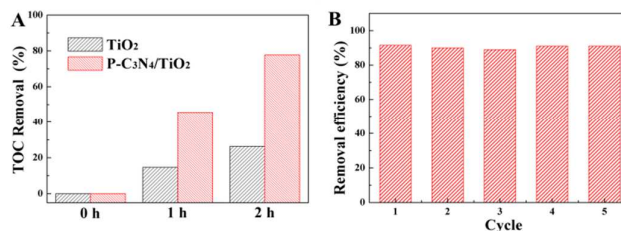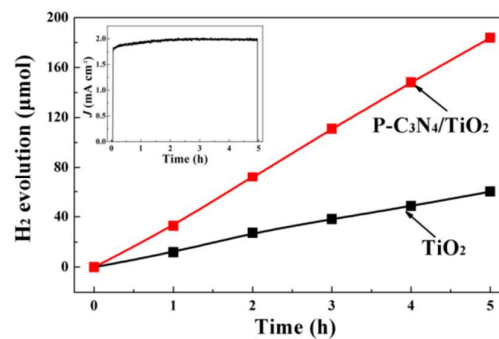

Figure 9 Time courses of hydrogen evolution for the P-C_3N_4/TiO_2 NTs and TiO_2 NTs electrodes at 0 V vs Ag/AgCl under illumination of simulated solar light

light (SI, Figure S11), showing good chemical stability of P-C_3N_4/TiO$_2$ NTs in the air.

Conclusions

P-C_3N_4/TiO$_2$ NTs was successfully synthesized by a facile method: electrochemical anodization and wet-dipping followed by a thermal polymerization. The prepared P-C_3N_4/TiO$_2$ NTs showed a remarkably enhanced photocurrent and improved photoconversion efficiency due to better charge separation and collection efficiency under solar light irradiation. Also, it showed much improved performance photoelectrocatalytic degradation of MB, with 2.7 times of degradation kinetic rate and 3.0 times TOC removal efficiency of pristine TiO$_2$, respectively. The prepared sample was further used for H$_2$ evolution, achieving a generation rate of 36.6 μmol h^{-1} cm^{-2} at 0 V vs Ag/AgCl with excellent stability up to 5 h. The composite materials are expected to have promising applications in photocatalysis, solar cells and other light harvesting devices.

Acknowledgements

Notes and references

1   P. Roy, S. Berger and P. Schmuki, *Angew. Chem. Int. Ed.*, 2011, **50**, 2904.
2   X. Quan, S. Yang, X. Ruan and H. Zhao, *Environ. Sci. Technol.*, 2005, **39**, 3770.
3   N. Lu, X. Quan, J. Li, S. Chen, H. Yu and G. Chen, *J. Phys. Chem. C*, 2007, **111**, 11836.
4   C. Liu, Y. Teng, R. Liu, S. Luo, Y. Tang, L. Chen and Q. Cai, *Carbon*, 2011, **49**, 5312.
5   Z. Zhang, Y. Yuan, G. Shi, Y. Fang, L. Liang, H. Ding and L. Jin, *Environ. Sci. Technol.*, 2007, **41**, 6259.
6   Y. Hou, X. Li, Q. Zhao, G. Chen and C. L. Raston, *Environ. Sci. Technol.*, 2012, **46**, 4042.
7   S. C. Hayden, N. K. Allam and M. A. El-Sayed, *J. Am. Chem. Soc.*, 2010, **132**, 14406.
8   J. H. Park, S. Kim and A. J. Bard, *Nano Lett.*, 2006, **6**, 24.
9   K. Shankar, J. I. Basham, N. K. Allam, O. K. Varghese, G. K. Mor, X. Feng, M. Paulose, J. A. Seabold, K.-S. Choi and C. A. Grimes, *J. Phys. Chem. C*, 2009, **113**, 6327.
10 H. Zhang, X. Quan, S. Chen, H. Yu and N. Ma, *Chem. Mater.*, 2009, **21**, 3090.
11 Z. Zhang, L. Zhang, M. N. Hedhili, H. Zhang and P. Wang, *Nano Lett.*, 2013, **13**, 14.
12 M. Ye, J. Gong, Y. Lai, C. Lin and Z. Lin, *J. Am. Chem. Soc.*, 2012, **134**, 15720.
13 G. K. Mor, K. Shankar, M. Paulose, O. K. Varghese and C. A. Grimes, *Nano Lett.*, 2006, **6**, 215.
14 D. K. Roh, W. S. Chi, H. Jeon, S. J. Kim and J. H. Kim, *Adv. Funct. Mater.*, 2014, **24**, 379.
15 O. K. Varghese, M. Paulose and C. A. Grimes, *Nat. Nanotechnol.*, 2009, **4**, 592.
16 K. Shankar, J. Bandara, M. Paulose, H. Wietasch, O. K. Varghese, G. K. Mor, T. J. Latempa, M. Thelakkat and C. A. Grimes, *Nano Lett.*, 2008, **8**, 1654.
17 R. Lü, W. Zhou, K. Shi, Y. Yang, L. Wang, K. Pan, C. Tian, Z. Ren and H. Fu, *Nanoscale*, 2013, **5**, 8569.
18 G. K. Mor, M. A. Carvalho, O. K. Varghese, M. V. Pishko and C. A. Grimes, *J. Mater. Res.*, 2004, **19**, 628.
19 S. Joo, I. Muto and N. Hara, *J. Electrochem. Soc.*, 2010, **157**, J221.
20 A. Zhang, M. Zhou, L. Han and Q. Zhou, *Appl. Catal. A: Gen.*, 2010, **385**, 114.
21 W. T. Sun, Y. Yu, H. Y. Pan, X. F. Gao, Q. Chen and L. M. Peng, *J. Am. Chem. Soc.*, 2008, **130**, 1124.
22 X. F. Gao, W. T. Sun, Z. D. Hu, G. Ai, Y. L. Zhang, S. Feng, F. Li and L. M. Peng, *J. Phys. Chem. C*, 2009, **113**, 20481.
23 G. Li, L. Wu, F. Li, P. Xu, D. Zhang and H. Li, *Nanoscale*, 2013, **5**, 2118.
24 H. Yang, W. Fan, A. Vaneski, A. S. Susha, W. Y. Teoh and A. L. Rogach, *Adv. Funct. Mater.*, 2012, **22**, 2821.
25 A. Kongkanand, K. Tvrdy, K. Takechi, M. Kuno and P. V. Kamat, *J. Am. Chem. Soc.*, 2008, **130**, 4007.
26 M. Wang, L. Sun, Z. Lin, J. Cai, K. Xie and C. Lin, *Energy Environ. Sci.*, 2013, **6**, 1211.
27 Y. Hou, X. Li, X. Zou, X. Quan and G. Chen, *Environ. Sci. Technol.*, 2008, **43**, 858.
28 A. I. Kontos, V. Likodimos, T. Stergiopoulos, D. S. Tsoukleris, P. Falaras, I. Rabias, G. Papavassiliou, D. Kim, J. Kunze and P. Schmuki, *Chem. Mater.*, 2009, **21**, 662.
29 S. Kuang, L. Yang, S. Luo and Q. Cai, *Appl. Surf. Sci.*, 2009, **255**, 7385.
30 Y. Hou, X. Li, Q. Zhao, X. Quan and G. Chen, *J. Mater. Chem.*, 2011, **21**, 18067.
31 Y. Hou, X. Y. Li, Q. D. Zhao, X. Quan and G. H. Chen, *Adv. Funct. Mater.*, 2010, **20**, 2165.
32 Q. Liu, J. He, T. Yao, Z. Sun, W. Cheng, S. He, Y. Xie, Y. Peng, H. Cheng, Y. Sun, Y. Jiang, F. Hu, Z. Xie, W. Yan, Z. Pan, Z. Wu and S. Wei, *Nat. Commun*, 2014, **5**, 5122.
33 X. Wang, K. Maeda, A. Thomas, K. Takanabe, G. Xin, J. M. Carlsson, K. Domen and M. Antonietti, *Nat. Mater.*, 2009, **8**, 76.
34 G. Liao, S. Chen, X. Quan, H. Yu and H. Zhao, *J. Mater. Chem.*, 2012, **22**, 2721.
35 J. Sun, J. Zhang, M. Zhang, M. Antonietti, X. Fu and X. Wang, *Nat. Commun.*, 2012, 1139.
36 J. Zhang, X. Chen, K. Takanabe, K. Maeda, K. Domen, J. D. Epping, X. Fu, M. Antonietti, and Wang X., *Angew. Chem.* 2010, **49**, 441.
37 C. Pan, J. Xu, Y. Wang, D. Li and Y. Zhu, *Adv. Funct. Mater.*, 2012, **22**, 1518.
38 S. C. Yan, S. B. Lv, Z. S. Li and Z. G. Zou, *Dalton Trans.*, 2010, **39**, 1488.
39 Y. Zhang and M. Antonietti, *Chem. Asian J.*, 2010, **5**, 1307.
40 Y. Zhang, T. Mori, J. Ye and M. Antonietti, *J. Am. Chem. Soc.*, 2010, **132**, 6294.
41 J. Zhang, G. Zhang, X. Chen, S. Lin, L. Mohlmann, G. Dolega, G. Lipner, M. Antonietti, S. Blechert and X. Wang, *Angew. Chem.*, 2012, **124**, 3237.
42 L. Yang, S. Luo, S. Liu, Q. Cai, Y. Xiao, S. Liu, F. Su and L. Wen, *J. Phys. Chem. C*, 2010, **114**, 4783.
43 D. Wang, Y. Liu, B. Yu, F. Zhou and W. Liu, *Chem. Mater.*, 2009, **21**, 1198.
44 Q. Xiang, J. Yu and M. Jaroniec, *J. Phys. Chem. C*, 2011, **115**, 7355.
45 S. Martha, A. Nashim and K. M. Parida, *J. Mater. Chem. A*, 2013, **1**, 7816.